International Journal of Heat and Technology
Vol. 44, No. 1, February, 2026, pp. 244-252
Journal homepage: http://iieta.org/journals/ijht

RSM-Based Optimization of MHD Radiative Ternary Hybrid Nanofluid (Ag–Cu–$MnZnFe_2O_4$) Flow over a Rotating Porous Disk with Thermal Relaxation and Chemical Reaction Effects

Charankumar Ganteda[1], G. Venkata Ramana Reddy[2], Vasavi Cheruku[3], Vanaja Kumari Ganji[4], Mousumi Bhanja[5*]

[1] Department of Mathematics, Siddhartha Academy of Higher Education, Deemed to be University, Vijayawada 520007, India
[2] Department of Mathematics, Koneru Lakshmaiah Education Foundation (KLEF), Vaddeswaram, Guntur 522302, India
[3] Department of Mathematics, Sreyas Institute of Engineering and Technology, Hyderabad 500068, India
[4] Department of Mathematics, Keshav Memorial Engineering College, Hyderabad 500058, India
[5] Department of Electronics and Telecommunication, Symbiosis Institute of Technology, Pune, Symbiosis International (Deemed University), Pune 412115, India

Corresponding Author Email: mousumi1988@yahoo.com

https://doi.org/10.18280/ijht.440121

Received: 9 December 2025
Revised: 6 February 2026
Accepted: 13 February 2026
Available online: 28 February 2026

Keywords:
Response Surface Methodology, hybrid nanofluid, rotating disk, thermal radiation, Runge–Kutta shooting method, thermal management

ABSTRACT

This study presents a comprehensive thermo-fluid analysis and statistical optimization of a ternary hybrid nanofluid (Ag–Cu–$MnZnFe_2O_4$ dispersed in kerosene) over a rotating porous disk under the coupled effects of magnetohydrodynamics (MHDs), thermal radiation, chemical reaction, and thermal relaxation. The novelty of this work lies in the integration of multi-physics hybrid nanofluid modeling with Response Surface Methodology (RSM) to quantify parameter interactions and optimize heat and mass transfer performance. The governing nonlinear boundary-layer equations are transformed using similarity variables and solved numerically via the Runge–Kutta shooting method. To enhance predictive capability, a Central Composite Design (CCD) is employed within the RSM framework to develop regression models for key engineering responses, including skin friction. ANOVA analysis confirms the statistical significance and adequacy of the developed models. The results indicate that increasing the magnetic parameter (M = 1–4) suppresses tangential velocity by 18–25% due to Lorentz drag, whereas thermal radiation (R = 0–2) enhances temperature by 14–17%. Higher thermal relaxation improves surface heat transfer by nearly 12%, while increasing Schmidt and reaction parameters reduces concentration profiles by up to 28%. Optimization results demonstrate the effectiveness of the ternary hybrid nanofluid for advanced cooling and rotating thermal systems.

1. INTRODUCTION

The present study examines the characteristics of temperature and flow of an Ag-Cu-$MnZnFe_2O_4$/Kerosene hybrid nanofluid in the vicinity of a rotating porous disc encompassing the consequences of chemical reaction, heat transfer, and magnetic fields. Similarity transformations were used to simplify the governing equations to ordinary differential equations, and the Runge-Kutta shooting method was used to solve the governing equations. Investigations demonstrated that thermal radiation increased the temperature by 14–17%, while enhancing the magnetic parameter reduced the tangential velocity by 18–25%. Elevating the Schmidt and chemical reaction parameters reduced mass concentration by 20–28%; however, accelerated thermal relaxation augmented the Nusselt number by 12%. In spinning systems, an increased Prandtl number led to a 15% decline in temperature, implying enhanced cooling efficiency. Prior research has investigated the thermodynamic and hydrodynamic characteristics of viscous fluid flow over spinning discs, emphasising the impacts of temperature and mass diffusion [1, 2].

Researchers acknowledged that nonlinear collaborations concerning outward temperature and attentiveness gradients diminish borderline sheet thickness, whereas considerable negative power index values may encourage increases in temperature and attentiveness outlines [3]. Few research efforts have aided in understanding the temperature and mass spread in non-Newtonian nanofluids, exploiting Cattaneo–Christov and Reiner–Rivlin simulations, highlighting the influences of thermophoresis and Brownian motion on heat and nanoparticle transport [4]. An investigational study directed the convective temperature transmission from a rotating disc, springy associations appropriate to Reynolds number and disc geometry, while neglecting the thermodynamic and hydrodynamic significances of Fourier-based fluxes [5]. Ternary hybrid nanofluids explored over a transferring developing disk beneath attractive and convective assumptions, performing a 10–15% heightening in Nusselt number duplicated to mono and hybrid nanofluids [6, 7].

Nanofluids have attracted extensive attention in recent years

due to their outstanding capability to develop heat transport implementation around several manufacturing and biomedical systems. Nanofluids concocted through scattering nanoparticles hooked on base liquids, display excellent thermophysical properties such as higher thermal conduction, developed viscosity, and developed convective temperature transport [8]. Their research expands the development of biomedical products of nanofluids, involving directed drug delivery, cancer therapy, and bio-imaging. Similarly, another study showed an all-inclusive appraisal of the success of nanofluids in educating heat transmission in the interior different attachments and thermal energy organizations, accentuating their standing in energy maintenance knowledges [9].

In the circumstances of thermal administration, researchers considered the role of nanofluids as next-generation coolants for electronic strategies. Their research showed that nanofluids require a more effective freezing machinery linked to established liquids, assisting in achieving consistency and efficiency in automated approaches [10]. These decisions have persuaded researchers to explore nanofluid behavior under diverse physical phenomena such as magnetic fields, thermal fallout, and substance outcomes, which are being explored in unconventional manufacturing and manufacturing approaches [11, 12].

In addition to these improvements, non-Newtonian liquids have developed a fundamental focus on liquid technicalities due to their complex rheological performance [13]. Including them, Casson fluid prototypes are extensively used to replicate viscoelastic materials such as blood, honey, and paints. A few researchers also explored the collective inspiration of thermal contamination and organic response on magnetohydrodynamic (MHD) Casson liquid movement past a perpendicular affecting permeable dish, presentation that radioactivity and response restrictions meaningfully disturb the velocity and temperature outlines [14-16]. In another study, similar assumptions concerning the interaction of magnetic and current impacts on Casson liquid movement are explored [17]. Continuing this exploration, the Soret and Dufour consequences in MHD Casson liquid pour, highlighting the prominence of temperature and mass assignment connection below the encouragement of contamination and organic response, is also explored [18, 19].

Furthermore, the geometrical constitution of the pour domain additionally plays a fundamental role in influencing the activities of non-Newtonian liquids [20]. Researchers observed the movement features of non-Newtonian liquids throughout a paraboloid of transformation and determined how the bend of the outside alters current models, temperature transport, and shear stress allocations. They highlighted the importance of complex geometries in the submissions of reasonable engineering and material processing [17]. The paper further observes that under moderate fields of magnetism, the skin friction decreases by 8%-12%, and this reveals substantial temperature and mass transference results in the system. Another researcher demonstrated the significance of a time-independent water-based hybrid nanofluid pour for controlling copper oxide and silver nanoparticles over a rotating disk. It discusses the influence of magnetic fields, thermophoresis, and other factors on the flow characteristics, emphasizing the enhanced heat transmission rates for hybrid nanofluid flow associated with nanofluid pour [21]. Some of the researchers have studied the properties of mass assignment and MHD Casson nanofluid thermal assignment on thermophoresis at the inactivity point, arithmetical reproduction of unstable MHD bio-convective current with Cattaneo-Christov thermal flux over an elongating exterior, mechanism of current emission, Soret-Dufour on ferromagnetic hybrid nanofluid over a porous exterior [22, 23]. Researchers investigated heat and mass transfer effects on Casson ternary hybrid nanofluid poured across an overextended revolutionary disk, incorporating non-linear assorted convection and a non-uniform temperature foundation/sink. Results show that the heat transmission rate for Casson ternary hybrid nanofluid increased by 2.98% compared to ternary hybrid nanofluid, and 7.49% and 6.89% higher than hybrid and conventional nanofluids, respectively [24, 25]. Additionally, the chemical reaction parameter has a positive impact on mass transmission rates. The dynamics of a ternary-hybrid nanofluid consisting of water with Copper (Cu), aluminum oxide (Al_2O_3), and Silver (Ag) nanoparticles, analyzing the effects of MHD stagnation-point stream and temperature transmission, is explored over a flat platter in an absorbing medium. It highlights the inspiration of considerations such as buoyancy, heat sources or sinks, and viscous forces on liquid movement and thermal transportation [26].

Existing literature thus identifies the gap in the direction of Fourier heat and mass fluxes on ternary hybrid nanofluid flow over a revolving permeable disk. Thus, this study explored the effects on the flow dynamics of hybrid nanofluids of magnetic fields, permeability, current emission, viscid indulgence, and biochemical reactions. This study further encompasses the computational simulations of critical parameters affecting velocity, concentration, Nusselt number, temperature, Sherwood number, and skin friction across the two permeable disks.

2. MATHEMATICAL FORMULATION OF THE PROBLEM

This research examined a steady, laminar, two-dimensional, and incompressible undercurrent of ternary hybrid nanofluid situated in a rotating permeable diskette as depicted in Figure 1. The analysis of heat transfer, along with mass transmission, was considered [12, 13]. The strategic flow was explored in a rotating circular porous disk with Ω as its angular velocity. T_w and C_w are considered close to the wall of the plate, while T_∞ and C_∞ are very far away from the disk, where fluid properties are not significant. Imposed on the turbulent stream is a compelling ground of uniform asset, while an attractive ground was ignored due to a very small Reynolds number.

The borderline sheet estimate is effective, and the governing equation for the tricky converts [20, 21]:

$$\frac{\partial u}{\partial r}+\frac{u}{r}+\frac{\partial w}{\partial z}=0 \tag{1}$$

$$\rho_{thnf}\left(u\frac{\partial u}{\partial r}-\frac{v^2}{r}+w\frac{\partial u}{\partial z}\right)+\frac{\partial p}{\partial r}=\mu_{hnf}\left(\frac{\partial^2 u}{\partial r^2}+\frac{1}{r}\frac{\partial u}{\partial r}-\frac{u}{r^2}+\frac{\partial^2 u}{\partial z^2}\right)-\sigma_{hnf}B_0^2u-\frac{\mu_{thnf}}{K_0}u \tag{2}$$

$$\rho_{thnf}\left(u\frac{\partial v}{\partial r}-\frac{uv}{r}+w\frac{\partial v}{\partial z}\right)=\mu_{thnf}\left(\frac{\partial^2 v}{\partial r^2}+\frac{1}{r}\frac{\partial v}{\partial r}-\frac{v}{r^2}+\frac{\partial^2 v}{\partial z^2}\right)-\sigma_{thnf}B_0^2v-\frac{\mu_{thnf}}{K_0}v \tag{3}$$

$$\rho_{thnf}\left(u\frac{\partial w}{\partial r}+w\frac{\partial w}{\partial z}\right)+\frac{\partial p}{\partial r}=\mu_{thnf}\left(\frac{\partial^2 w}{\partial r^2}+\frac{1}{r}\frac{\partial w}{\partial r}+\frac{\partial^2 w}{\partial z^2}\right) \quad (4)$$

$$\left(\rho c_p\right)_{thnf}\left(u\frac{\partial T}{\partial r}+w\frac{\partial T}{\partial z}\right)+\frac{\partial p}{\partial r}=K_{thnf}\left(\frac{\partial^2 T}{\partial r^2}+\frac{1}{r}\frac{\partial T}{\partial r}+\frac{\partial^2 T}{\partial z^2}\right)-\frac{\partial q_r}{\partial z}+Q_0(T-T_\infty)+\frac{\mu_{thnf}}{\left(\rho c_p\right)_{thnf}}\left(\frac{\partial u}{\partial z}\right)^2-\Gamma_1\left(u^2\frac{\partial^2 T}{\partial r^2}+w^2\frac{\partial^2 T}{\partial r^2}+2uw\frac{\partial^2 T}{\partial r\partial z}+\left(u\frac{\partial u}{\partial r}+w\frac{\partial w}{\partial r}\right)\frac{\partial T}{\partial r}+\left(u\frac{\partial u}{\partial r}+w\frac{\partial w}{\partial r}\right)\frac{\partial T}{\partial z}\right)+\sigma_{thnf}B_0^2 v \quad (5)$$

$$\left(u\frac{\partial C}{\partial r}+w\frac{\partial C}{\partial z}\right)=D_M\left(\frac{\partial^2 C}{\partial r^2}+\frac{1}{r}\frac{\partial C}{\partial r}+\frac{\partial^2 C}{\partial z^2}\right)-K_l(C-C_\infty) \quad (6)$$

Subject to the borderline circumstances:

$$u=0, v=\Omega r, w=w_0, T=T_w, C=C_w \text{ at } z=0$$
$$u\longrightarrow 0, v\longrightarrow 0, T\longrightarrow T_\infty, P\longrightarrow P_\infty, C\longrightarrow C_\infty \text{ at } z\longrightarrow\infty \quad (7)$$

To assess the radiative thermal flux, Rosseland dispersal estimate as labelled in the study of Kataria and Patel [22] as:

$$q_r=-\frac{4\sigma^*}{3K^*}\frac{\partial T^4}{\partial z} \quad (8)$$

somewhere, σ* denotes the Stefan-Boltzmann constant, and K* signifies the factor of average captivation. By positing the hypothesis that the disparate temperatures present within the flow are exceedingly minimal, it follows that T^4 can be articulated in a nonlinear representation as:

$$\frac{\partial q_r}{\partial z}=\frac{\partial}{\partial z}\left(\frac{4\sigma^*}{3K^*}4T^3\frac{\partial T}{\partial z}\right) \quad (9)$$

To streamline the leading PDEs, appropriate representations of the revolution variable star are practical. These variable quantities are:

$$u=r\Omega f', \mathrm{v}=\mathrm{r}\Omega g, \mathrm{w}=\sqrt{2\Omega\nu_f}f, P=P_\infty+2\Omega\mu_f P(\eta), \eta=\sqrt{\frac{2\Omega}{\nu_f}}z, \theta=\frac{T-T_\infty}{T_w-T_\infty} \quad (10)$$

Using the equation above, we can create a dimensionless form of the equations:

$$\frac{A_1}{A_4}(2ff''-(f')^2+g^2)+2f'''-\frac{A_5}{A_4}Mf'-\frac{1}{K}f'=0 \quad (11)$$

$$\frac{A_1}{A_4}(2fg'-2f'g)+2g''-\frac{A_5}{A_4}Mf'-\frac{1}{K}f'=0 \quad (12)$$

$$\frac{A_2}{A_3}f\theta'+\frac{1}{Pr}\left(\theta''+\frac{4R}{3A_3}\frac{d}{d\eta}\left(1+\theta(\eta)(\theta_w-1)\right)^3\frac{d\theta(\eta)}{d\eta}\right)+\frac{A_2}{A_3}f\theta'+PrQr(f^2\theta''+ff'\theta')+Q\theta+Ec(f'')^2+EcM(f')^2=0 \quad (13)$$

$$\phi''-KrSc\phi-Sc\phi' f=0 \quad (14)$$

Subject to:

$$\begin{cases} f=-S, f'=0, g=1, \theta=1, C=1 \text{ at } \eta=0 \\ f'\longrightarrow 0, g\longrightarrow 0, \theta\longrightarrow 0, \phi\longrightarrow 0 \text{ at } \eta\longrightarrow\infty \end{cases} \quad (15)$$

where, $A_1=\frac{\rho_{hnf}}{\rho_f}$, $A_2=\frac{\left(\rho c_p\right)_{hnf}}{\left(\rho c_p\right)_f}$, $A_3=\frac{K_{hnf}}{K_f}$, $A_4=\frac{\mu_{hnf}}{\mu_f}$, $A_5=\frac{\sigma_{hnf}}{\sigma_f}$, attractive restriction $M=\frac{\sigma_f B_0^2}{\Omega\rho_f}$, current emission $R=\frac{4\alpha^* T_\infty^3}{3K^*K_f}$, heat proportion restriction $\theta_w=\frac{T_w}{T_\infty}$, Prandtl number $Pr=\frac{\mu_f\left(\rho c_p\right)_f}{\rho_f K_f}$, current reduction restriction $Q_r=2\Gamma_1\Omega$, heat production restriction $Q=\frac{Q_0}{\Omega\left(\rho c_p\right)_f}$, Eckert quantity is $Ec=\frac{(\Omega)^2}{c_p(T_w-T_\infty)}$.

The measures of manufacturing attention are demarcated for C_g, C_f with Nu correspondingly.

$$C_g=\left(\frac{(1-\phi_1-\phi_2-\phi_3)^{-2.5}}{(1-\phi_1-\phi_2-\phi_3)+\phi_1\left(\frac{\rho_1}{\rho_f}\right)}+\phi_2\left(\frac{\rho_2}{\rho_f}\right)+\phi_3\left(\frac{\rho_3}{\rho_f}\right)\right)g'(0)$$

$$C_f=\left(\frac{(1-\phi_1-\phi_2-\phi_3)^{-2.5}}{(1-\phi_1-\phi_2-\phi_3)+\phi_1\left(\frac{\rho_1}{\rho_f}\right)}+\phi_2\left(\frac{\rho_2}{\rho_f}\right)+\phi_3\left(\frac{\rho_3}{\rho_f}\right)\right)f''(0)$$

$$Nu=\frac{Nu}{\sqrt{Re_z}}=\frac{K_{hnf}}{K_f}\left(1+\frac{4Nr}{4M_3}(1+(\theta_w-1)\theta(0))^3\right)\theta'(0)$$

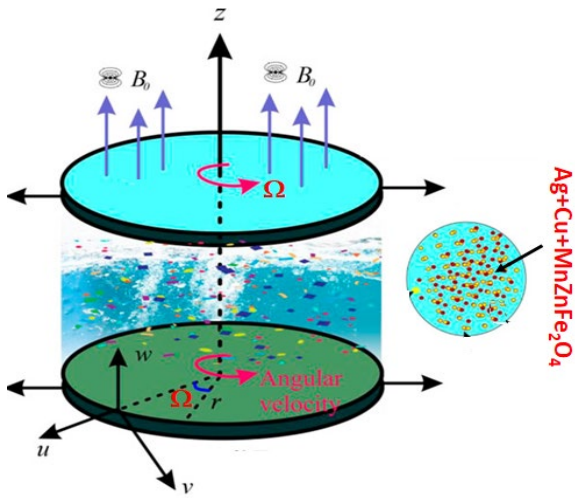

Figure 1. Physical configuration

3. RESULTS AND DISCUSSION

This scholarly inquiry addresses the systems of transformed Eqs. (11)-(14) in conjunction with (15) by utilizing the Runge-Kutta methodology in tandem with the shooting method. The baseline values for the control parameters are specified as in Table 1. This study provides a graphic representation of the influence of all flow factors. The assigned parameter values are consistently applied in all numerical computations unless stated otherwise. This research also presents graphical illustrations showing the effects of various flow parameters on system behavior.

Figure 2 indicates that a higher thermal radiation parameter (R) yields a higher fluid temperature of 16% as the boundary layer takes in and gives back the heat, and the Nusselt number decreases by 13%, demonstrating lesser temperature variation at the circular surface. As shown in Figure 3, the permeability parameter K increases by 18% when 0.5 changes to 1.5 because the higher the porosity, the less the resistance to flow,

and the easier the fluid flows through the disk. This, in turn, made the convective motion in the boundary layer stronger. But this higher permeability also causes nanoparticles to move around randomly and collide with each other, which has a small effect on the uniformity of temperature and concentration distributions. Figure 4 shows that raising the heat generation parameter Q from 0 to 2 raises the fluid temperature by up to 22% and makes the thermal boundary layer thicker. The heat source gives the fluid internal energy, which makes the nanofluid and speeds up the thermal dispersion rate. The results indicate a 9–11% decrease in the Nusselt number as Q increases, which is consistent with the general pattern of lower surface thermal gradients caused by adding heat to a volume.

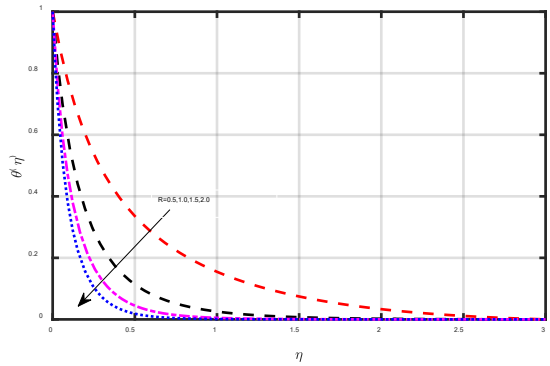

Figure 2. Consequences of current emissions on the thermal outlines

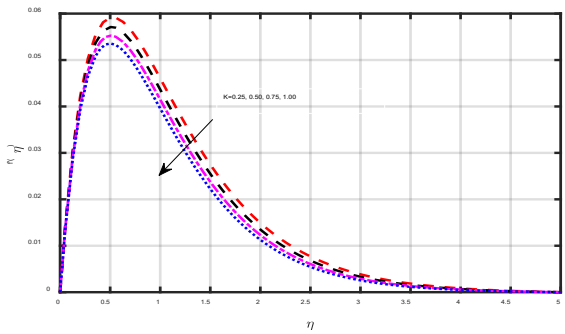

Figure 3. Consequence of permeability restriction on the radial speed outlines

The conclusions deliver positive comprehensions for enhancing MHD movement performance in machinery like thermal regulation of spinning apparatus and electromagnetic braking processes, near the disk, thermal strengthening. This process makes the material more thermally conductive and makes the particles move around more. The formation of electromagnetic fields can be attributed to the interaction between the electric field and the magnetic force, as observed in the context of a point charge, which ultimately gives rise to this electromagnetic phenomenon. As a result, it has been concluded that the electromagnetic force serves to restrain the fluid's movement by lessening momentum within the boundary layer, which consequently leads to a decline in fluid velocity.

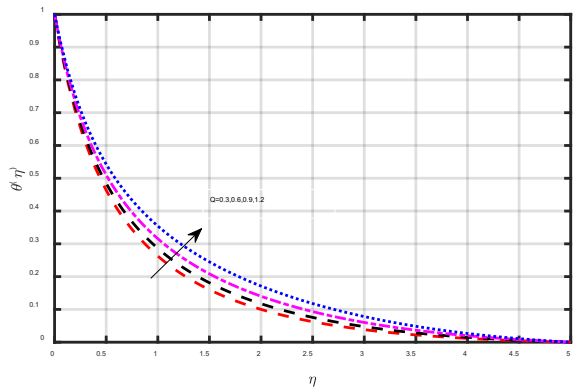

Figure 4. Consequence of heat source restriction on the heat outlines

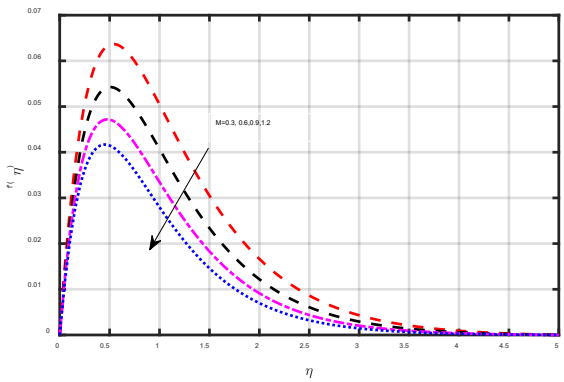

Figure 5. Consequences of the magnetic parameter on the circular momentum shapes

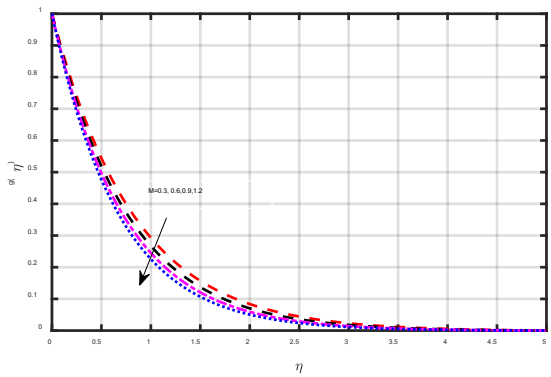

Figure 6. Consequence of the magnetic parameter on the tangential momentum outlines

Table 1. Thermophysical properties of nanomaterials

Belongings	Current Conduction	Temperature Capability	Compactness	Prandtl Number
Silver (Ag)	429	235	10,50	-
Copper (Cu)	401	385	8933	-
$MnZnFe_2O_4$	3.9	1050	4700	-
Kerosene oil	0.15	2090	783	21

Figures 5 and 6 show that changing the magnetic parameter M from 1 to 4 causes the radial and tangential velocity profiles to drop by 22% and 25%, respectively. This is because Lorentz forces are created that push against the movement of conducting nanofluid particles when a transverse magnetic field is present. The electromagnetic damping effect makes it harder for momentum to move and makes the momentum boundary layer thicker. The skin friction coefficient along the disk surface increased by 17%, which means that magnetic resistance caused more viscous drag.

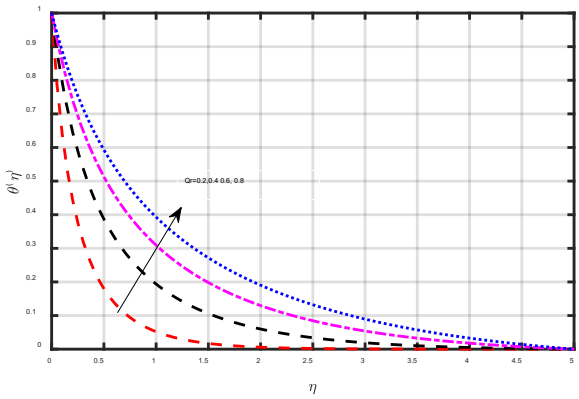

Figure 7. The temperature outlines are the outcome of the warmth relaxation restriction

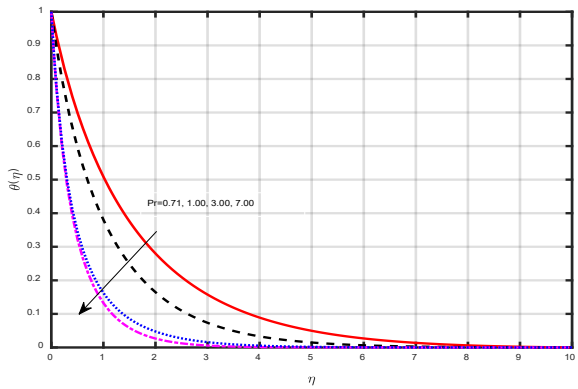

Figure 8. The Prandtl number is important for the temperature outlines

Figure 7 explores the role of the thermal relaxation parameter γ, which arises from the Cattaneo–Christov heat flux model [27-29], accounting for finite speed of heat propagation. An increase in γ(from 0.2 to 0.8) leads to a 14% increase in fluid temperature, reflecting a delayed response in heat flux adjustment with respect to temperature gradients. This increases the depth of thermal penetration and reduces thermal wave dissipation. Furthermore, it improves the temperature stability of the fluid by smoothing abrupt thermal gradients, a feature desirable in high-speed rotating systems and non-Fourier heat conduction modeling. Figure 8 reveals that increasing the Prandtl number (from 5 to 8) significantly decreases the fluid temperature by approximately 15%. Higher values of Pr, which is the ratio of momentum diffusivity to thermal dispersion, show that momentum diffusion predominates and limits thermal diffusivity. Subsequently, the thermal barrier layer converts thinner, and the exterior temperature flux progresses. Better convective warm communication is denoted by an 11% enhance in the Nusselt number. This highlight is needed in thermal administration approaches that use oils or other high-Pr liquids, where speedy momentum transport without substantial thermal transference needs to be accomplished.

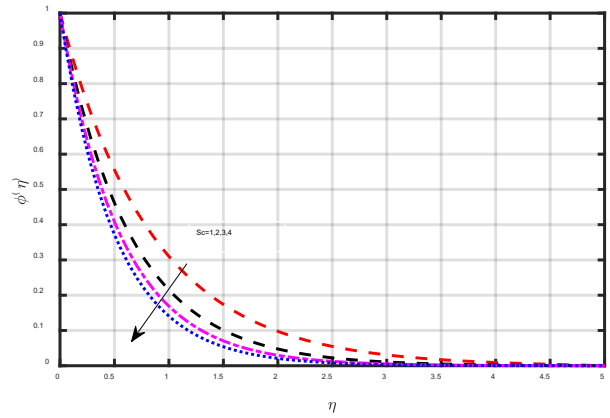

Figure 9. Schmidt number's importance in relation to attentiveness describes

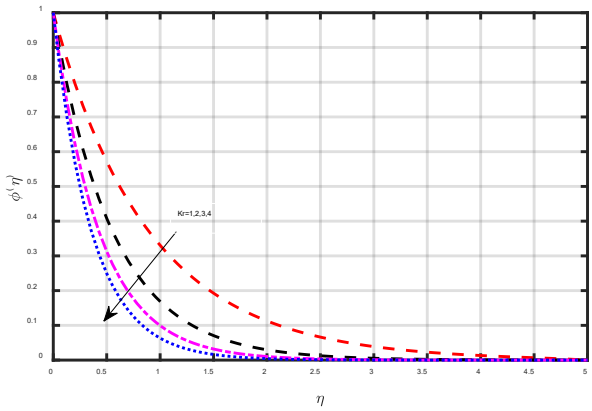

Figure 10. The temperature indicates the biological response's consequences

Figure 9 shows the consequence of the Schmidt number (Sc), which identifies momentum diffusivity as the result of mass diffusivity. As the solute species or nanoparticles occupy privileged mass distribution in the liquid, the absorption outline decreases by up to 28% as Sc increases (between 1 and 3). A contracted intensity borderline sheet develops in higher Sc, representing extra-significant sticky influences than mass diffusion. A 12–15% upsurge in the Sherwood number specifies steeper awareness angles at the disk advance, which is precious for improvements requiring precise genus monitor. Figure 10 establishes that floating the biological response constraint K_1 from 0 to 2 decreases both meditation and rapidity by about 20%, brilliant reactant ingesting in the borderline sheet, and the connection between mass diffusion and impetus transportation [30, 31]. These decisions are influential for demonstrating responsive nanofluid movements in polymer, therapeutic, and catalysis presentations. Ternary hybrid nanofluids establish superior temperature transfer, with the demonstration realizing a 12–15% enhance in Nusselt number over hybrid nanofluids and up to 18% associated with conservative single-phase liquids. The synergistic effect of the merged nanoparticle organisation, where high thermal conductivity (Ag, Cu) and magnetic response ($MnZnFe_2O_4$)

accurately associate, is accountable for this improved thermal implementation.

4. RESPONSE SURFACE METHODOLOGY

An actual technique for generating experiential correlations concerning a wide range of relevant characteristics is the Response Surface Methodology (RSM). When it permits one to examine the stored components that exhibit the minimum and largest effect on the productions, it's great for assessing procedures with a lot of moving parts. The goal of RSM is response optimisation, and this study determines the impact of selected input parameters, specifically β, α, and Ec on Skin friction. Table 2 demonstrates the manipulation of the input parameters at three distinct levels and within a specific range.

$$Skin\ Friction = Z_0 + Z_1\beta + Z_2\alpha + Z_3 Ec + Z_{11}\beta^2 + Z_{22}\alpha^2 + Z_{33}Ec^2 + Z_{12}\beta * \alpha + Z_{13}\alpha * Ec + Z_{14}Ec * \beta$$

$$(-f''(0)) = 0.9954 + 0.2704\ \beta + 0.06352\ \alpha - 0.0817\ Ec$$

The residual plot is given in Figure 11. In the residual plot, the difference observed from the scattered plot and the predicted y-value is known as a residual. According to the figure, the normal probability plot is in good condition because all the points are near the approximate straight lines that represent normality. In the residual histogram, splits do not appear as a mirror image, so there is a skewed proportioned distribution. Observed and fitted values exhibit a good correlation if associated with the residual graph and tailored value.

When you look at the results, β and α both have a positive slope, which means fluid elasticity and stretching really boost wall shear stress. On the other hand, Ec has a negative slope, so viscous dissipation cuts down the skin friction. Out of all these factors, β and α stand out; they impact things way more than Ec does, and you can see that from the steeper slopes in the main effects plot in Figure 12. Figure 13 determines 3D surface plots of the skin friction coefficient, -f''(0), varying with the important parameters, b, a, and Eckert number Ec. In both plots, you can observe the interplay between two of these parameters to influence the skin friction, and the third parameter remains constant.

Table 2. Response values of (−f″(0))

Real Values			Response
β	α	Ec	(−f″ (0))
0.5	2	1	1.193
0.25	1	0.5	1.0946
0.5	1	0.5	1.1668
0.25	2	0.5	1.1265
0	1	0.5	1.0297
0.25	1	0	1.1289
0.5	2	0	1.2627
0.25	1	1	1.0396
0	0	1	0.9204
0.5	0	1	1.0378
0.25	1	0.5	1.0946
0	0	0	1.0005
0.5	0	0	1.128
0.25	1	0.5	1.0221
0.25	0	0.5	1.0221
0.25	1	0.5	1.0946
0	2	1	1.0413
0.25	1	0.5	1.0946
0.25	1	0.5	1.0946
0	2	0	1.1205

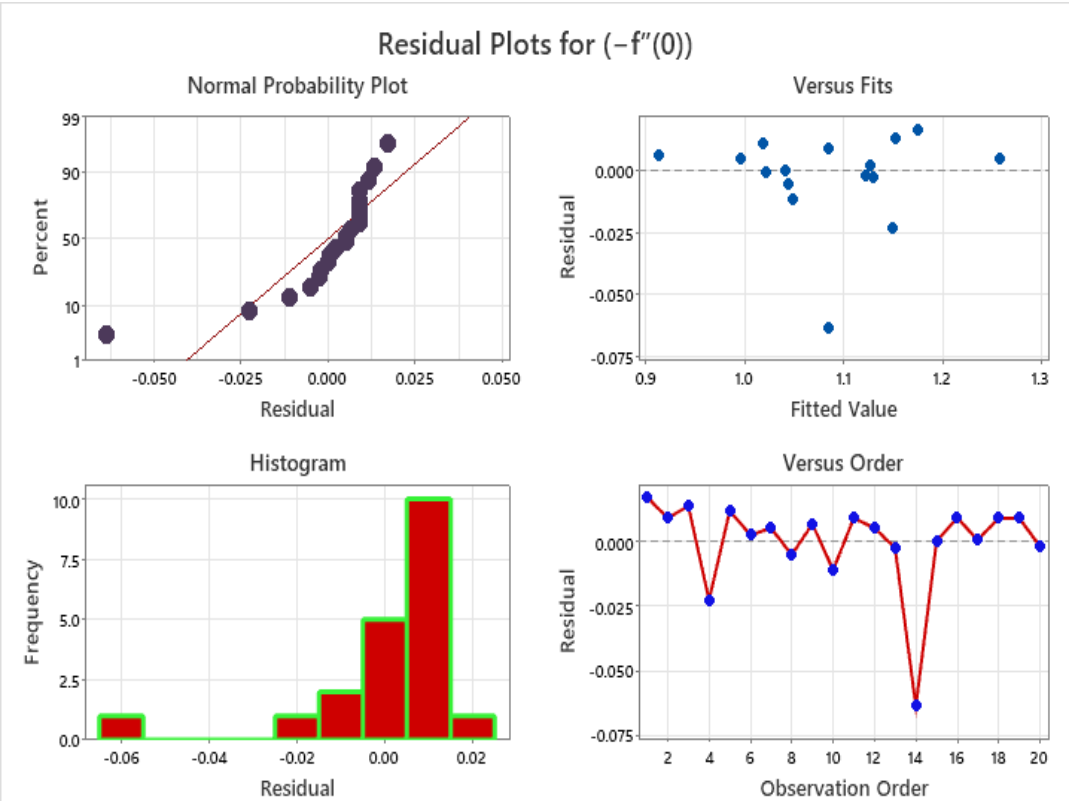

Figure 11. Plot of residual vs. observation for skin friction

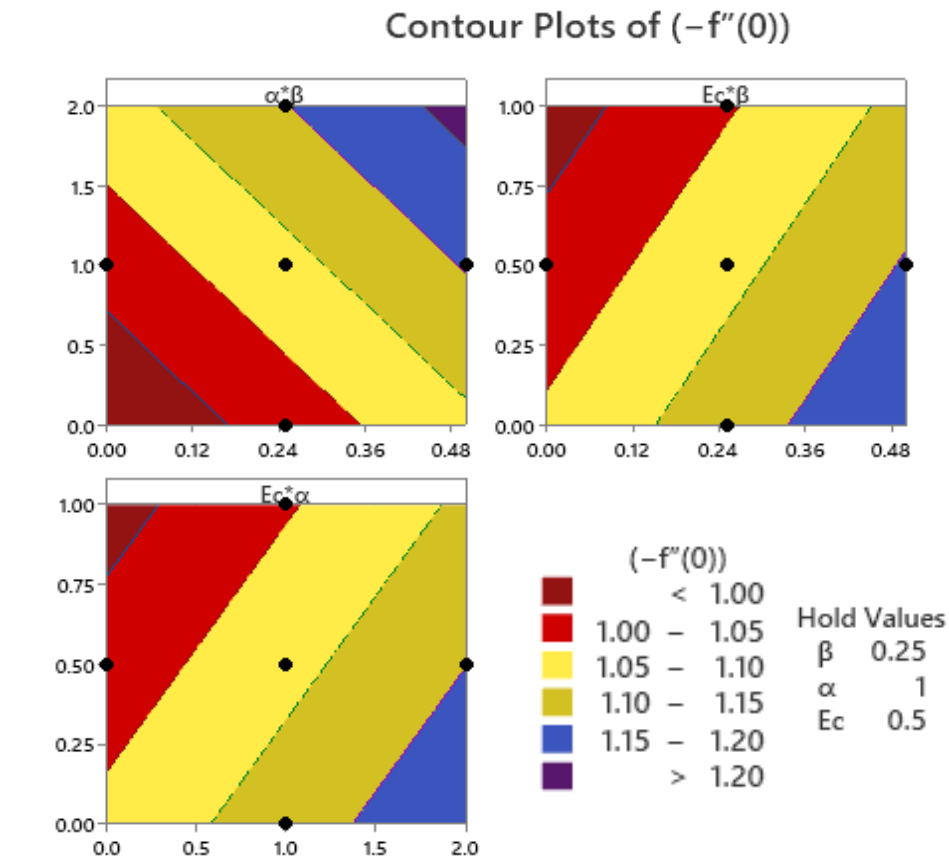

Figure 12. For various parameter interactions, contour plots (a) through (c) illustrate skin friction

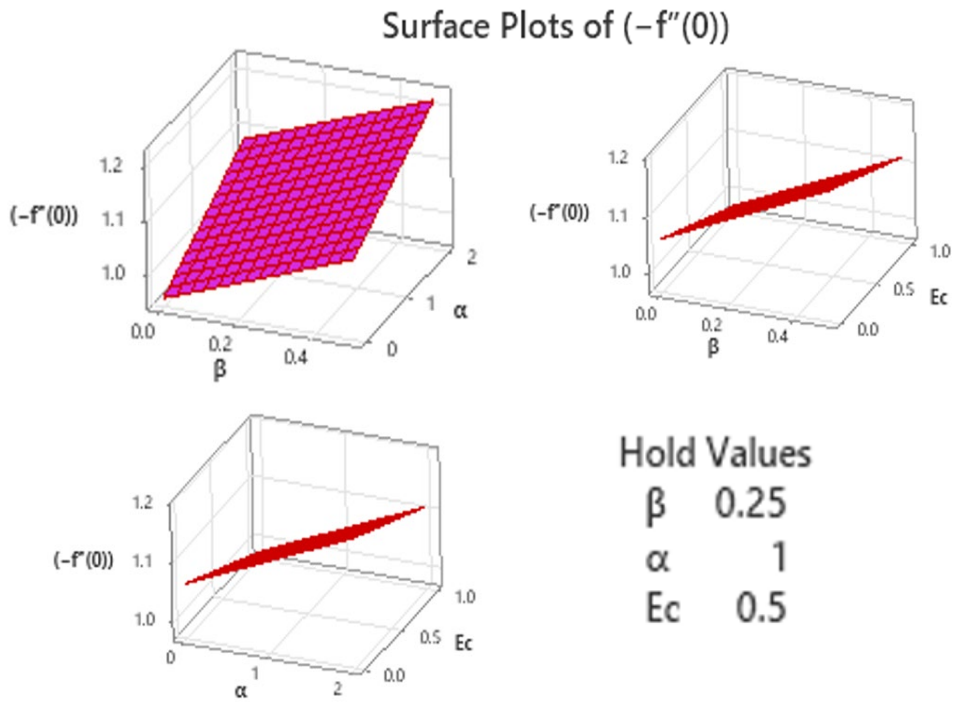

Figure 13. Surface plots of skin friction coefficient $-f''(0)$ for varying physical parameters

5. CONCLUSIONS

This study examined the thermodynamic and hydrodynamic nature of a ternary hybrid nanofluid (Ag-Cu-$MnZnFe_2O_4$/kerosene) in a rotating porous disk, considering the combined effects of magnetic field, thermal radiation, chemical reaction, and thermal relaxation. The findings indicate that the magnetic parameter plays a profound role in

inhibiting the radial and tangential velocities under the influence of the Lorentz force, whereas the thermal radiation and relaxation are two mechanisms that promote the temperature distribution. Increasing the Schmidt number and reaction parameter decreases concentration profiles, which shows that it has greater control over mass diffusion. An increase in Prandtl numbers reduces temperature differences, which implies enhanced cooling efficiency. The main value of the work is the combined approach to the modeling of ternary hybrid nanofluid flow on the basis of a rotating porous disk and the simultaneous approach to Fourier and radiative heat flux, which allows understanding the characteristic features of rotating thermal systems and modern cooling equipment. The study, however, makes assumptions based on the laminar flow, constant thermophysical properties and does not include the nanoparticle aggregation and experimental validation. Future studies can implement the properties of the variables, non-Fourier heat flux models, turbulence, experimental, or data-based optimization techniques to increase the practicality of the application and predictive performance.

REFERENCES

[1] Rehman, S.U., Mariam, A., Ullah, A., Asjad, M.I., Bajuri, M.Y., Pansera, B.A., Ahmadian, A. (2021). Numerical computation of buoyancy and radiation effects on MHD micropolar nanofluid flow over a stretching/shrinking sheet with heat source. Case Studies in Thermal Engineering, 25: 100867. https://doi.org/10.1016/j.csite.2021.100867

[2] Srinivas, G., Babu, B.S., Goud, B.S. (2024). SLIP effects on heat and mass transfer through CuO-water nanofluid in a horizontal channel heated at center. Journal of Thermal Analysis and Calorimetry, 149(22): 13267-13283. https://doi.org/10.1007/s10973-024-13686-4

[3] Bangerth, S., Tiwari, R., Shooshtari, A., Ohadi, M. (2019). Heat/mass transfer enhancement of an exothermic absorption utilizing a spinning disk reactor. International Journal of Heat and Mass Transfer, 129: 326-341. https://doi.org/10.1016/j.ijheatmasstransfer.2018.08.064

[4] Mushtaq, A., Mustafa, M. (2017). Computations for nanofluid flow near a stretchable rotating disk with axial magnetic field and convective conditions. Results in Physics, 7: 3137-3144. https://doi.org/10.1016/j.rinp.2017.08.031

[5] Kumar, M., Mondal, P.K. (2022). Irreversibility analysis of hybrid nanofluid flow over a rotating disk: Effect of thermal radiation and magnetic field. Colloids and Surfaces A: Physicochemical and Engineering Aspects, 635: 128077. https://doi.org/10.1016/j.colsurfa.2021.128077

[6] Mabood, F., Mackolil, J., Mahanthesh, B., Rauf, A., Shehzad, S.A. (2021). Dynamics of Sutterby fluid flow due to a spinning stretching disk with non-Fourier/Fick heat and mass flux models. Applied Mathematics and Mechanics-English Edition, 42(9): 1247-1258. https://doi.org/10.1007/S10483-021-2770-9

[7] Bilal, M., Khan Marwat, D.N., Alam, A. (2022). Diffusion of heat and mass in flow of viscous fluid over a moving porous and rotating disk. Advances in Mechanical Engineering, 14(8): 168781322211199. https://doi.org/10.1177/16878132221119917

[8] Moatimid, G.M., Mohamed, M.A.A., Elagamy, K. (2022). Heat and mass flux through a Reiner–Rivlin nanofluid flow past a spinning stretching disc: Cattaneo–Christov model. Dental Science Reports, 12(1). https://doi.org/10.1038/s41598-022-18609-7

[9] Iguchi, A., Komori, K., Izumi, R. (1974). Heat and mass transfer from a rotating disk with a source flow. JSME International Journal Series B-Fluids and Thermal Engineering, 17(113): 1476-1485. https://doi.org/10.1299/JSME1958.17.1476

[10] Usman, U., Kumar, R., Khan, W.A., Al-lobani, E.M., Massoud, E.E.S. (2025). Mathematical modeling and numerical simulations of convective heat transport in a stagnant flow of water-based copper, aluminum oxide and MWCNTs nanofluid upon a stretching spinning disk. Journal of Applied Mathematics and Mechanics, 105(1). https://doi.org/10.1002/zamm.202400476

[11] Dasore, A., Tarun, P., Ramakrishna, K., Naveen, P. (2020). Convective hot air-drying kinetics of red beetroot in thin layers. Frontiers in Heat and Mass Transfer, 14: 1-8. https://doi.org/10.5098/hmt.14.23

[12] Yasmin, H., Al-Essa, L.A., Mahnashi, A.M., Hamali, W., Anwar, S. (2024). A magnetohydrodynamic flow of a water-based hybrid nanofluid past a convectively heated rotating disk surface: A passive control of nanoparticles. Reviews on Advanced Materials Science, 63(1). https://doi.org/10.1515/rams-2024-0054

[13] Tejes, P.K.S., Naik, B.K., Dasore, A., Hashim, N. (2025). Multi-objective optimization of a three-fluid hollow fiber membrane dehumidifier for energy-efficient drying applications. Case Studies in Thermal Engineering, 75: 107036. https://doi.org/10.1016/j.csite.2025.107036

[14] Swain, B.K. (2023). Dynamics of ternary-hybrid nanofluid of water conveying copper, alumina and silver nanoparticles when entropy generation, viscous dissipation, Lorentz force are significant. Journal of Applied Mathematics and Mechanics. https://doi.org/10.1002/zamm.202200254

[15] Konijeti, R., Dasore, A., Rajak, U. Rajan, K., Abhishek, S., Anil, S.Y. (2024). CFD analysis of heat transfer by free convection over a vertical cylinder with circular fins of triangular cross-section. Multiscale and Multidisciplinary Modeling, Experiments and Design, 7: 741-753. https://doi.org/10.1007/s41939-023-00237-x

[16] Reddy, K.J., Madhusudhana R.N.P., Konijeti, R., Abhishek, D. (2018). Numerical investigation of chemical reaction and heat source on radiating MHD stagnation point flow of Carreau nanofluid with suction/injection. Defect and Diffusion Forum, 388: 171-189. https://doi.org/10.4028/www.scientific.net/DDF.388.171

[17] Rafique, E., Iram, A., Jahan, S., Sohail, M., Sherif, E.S.M. (2025). Bio-convective flow of non-Newtonian Williamson nanofluid model with heat generation and thermal radiation aspects past over a stretched porous sheet via OHAM. Multiscale and Multidisciplinary Modeling, Experiments and Design, 8: 45. https://doi.org/10.1007/s41939-024-00596-z

[18] Dasore, A., Konijeti, R., Prakash, B.O., Balram, Y. (2024). Numerical and empirical simulation of fluid flow in a spiral plate heat exchanger with Nusselt number correlation development. International Journal on Interactive Design and Manufacturing (IJIDeM), 18:

3103-3113. https://doi.org/10.1007/s12008-023-01454-x
[19] Ullah, Z., Said, M.A., Alsulami, M.D., Al Arni, S., Eljaneid, N.H.E., Hakami, A., Ben Khedher, N. (2024). Thermal radiation and Soret/Dufour effects on amplitude and oscillating frequency of Darcian mixed convective heat and mass rate of nanofluid along porous plate. Case Studies in Thermal Engineering, 59: 104562. https://doi.org/10.1016/j.csite.2024.104562
[20] Dasore, A., Ramakrishna, K., Naik, B.K. (2020). Evaluation of heat and mass transfer coefficients at beetroot–air interface during convective drying. Interfacial Phenomena and Heat Transfer, 8(4): 303-319. https://doi.org/10.1615/InterfacPhenomHeatTransfer.2020036455
[21] Sandhya, A., Reddy, G., Deekshitulu, G.V.S.R. (2020). Radiation and chemical reaction effects on MHD Casson fluid flow past a semi-infinite vertical moving porous plate. Indian Journal of Pure & Applied Physics, 58: 548-557.
[22] Kataria, H.R., Patel, H.R. (2016). Radiation and chemical reaction effects on MHD Casson fluid flow past an oscillating vertical plate embedded in porous medium. Alexandria Engineering Journal, 55(1): 583-595. https://doi.org/10.1016/j.aej.2016.01.019
[23] Suresh Babu, B., Cheruku, V., Vanaja Kumari, G., Shamshuddin, M.D. (2025). Exploring heat mass transmission on immiscible fluid flow due to vertical channel with independent multiple slip effects: Computational work. Modern Physics Letters B, 39(32). https://doi.org/10.1142/s0217984925501969
[24] Moita, A., Moreira, A., Pereira, J. (2021). Nanofluids for the next generation thermal management of electronics: A review. Symmetry, 13(8): 1362. https://doi.org/10.3390/sym13081362
[25] Babu, B.S., Srinivas, G., Gosty, V., Kumari, G.V. (2024). Numerical analysis of slip phenomena on heat and mass transfer in a vertical channel with immiscible fluids with variable viscosity and thermal conductivity. Heat and Mass Transfer, 61(1). https://doi.org/10.1007/s00231-024-03532-6
[26] Abbas, S., Ahmad, M., Nazar, M., Ahmad, Z., Amjad, M., Al Garalleh, H., Jan, A.Z. (2024). Soret effect on MHD Casson fluid over an accelerated plate with the help of constant proportional Caputo fractional derivative. ACS Omega, 9(9): 10220-10232. https://doi.org/10.1021/acsomega.3c07311
[27] Lavanya, B., Srinivas, G., Babu, B.S., Makinde, O.D. (2025). Numerical analysis of heat transfer of CuO-water nanofluid through a square channel with heated inner triangular groove. Archives of Thermodynamics. https://doi.org/10.24425/ather.2025.154183
[28] Vemanaboina, H., Yelamasetti, B., Panchagnula, J.S., Kilari, N., Prakash, C., Kumar, S., Mehdi, H. (2025). Thermal and mechanical analysis of C-276 alloy using CO_2 laser beam welding process. Transactions of the Indian Institute of Metals, 78(2). https://doi.org/10.1007/s12666-024-03476-9
[29] Reddy, K.S., Purushotham, A., Kala, K.L., Gupta, M.S., Kumar, P.K., Vemanaboina, H. (2023). Thermal mapping of SS316L experimental and simulation for GTA welding process with moving heat source model using FEA. International Journal on Interactive Design and Manufacturing (IJIDeM), 18(5): 2755-2763. https://doi.org/10.1007/s12008-023-01310-y
[30] Gosty, V., Srinivas, G., Babu, B.S., Goud, B.S., Hendy, A.S., Ali, M.R. (2024). Influence of variable viscosity and slip on heat and mass transfer of immiscible fluids in a vertical channel. Case Studies in Thermal Engineering, 58: 104368. https://doi.org/10.1016/j.csite.2024.104368
[31] Jyothi, K., Maditham, V., Ramavat, G., Vemanaboina, H., Kantipudi, M.V.V.P. (2025). Thermal–Solutal dynamics between rotating disks in bio-stabilised ZnO hybrid nanofluids: Coupled FEM and neural network analysis. International Journal of Heat and Technology, 43(6): 2350-2358. https://doi.org/10.18280/ijht.430632